Materials Today Bio 24 (2024) 100904

Contents lists available at ScienceDirect

Materials Today Bio

journal homepage: www.journals.elsevier.com/materials-today-bio

A follicle-stimulating hormone receptor-targeted near-infrared fluorescent probe for tumor-selective imaging and photothermal therapy

Qiyu Liu [a,1], Tao Pu [a,b,c,1], Xiaobo Zhou [d,1], Jiaan Sun [a], Wei Yuan [d], Sidi Zhang [d], Mingxing Zhang [a], Meng Zhang [a], Jing Peng [a], Fuyou Li [d,***], Xiaoyan Zhang [a,b,c,**], Congjian Xu [a,b,c,*]

[a] Obstetrics and Gynecology Hospital of Fudan University, Shanghai, 200011, China
[b] Shanghai Key Laboratory of Female Reproductive Endocrine Related Diseases, Shanghai, 200011, China
[c] Department of Obstetrics and Gynecology of Shanghai Medical School, Fudan University, Shanghai, 200032, China
[d] Department of Chemistry, Fudan University, Shanghai, 200438, China

ARTICLE INFO

Keywords:
Ovarian cancer
Follicle-stimulating hormone
Targeted imaging
Photothermal therapy

ABSTRACT

Late detection, peritoneal dissemination, chemoresistance and weak response to targeted therapeutics lead to high mortality in ovarian cancer. More efficient and specific tumor imaging and therapeutic agents are needed to improve the resection rate of surgery and to eliminate residual disease. The expression patterns of follicle-stimulating hormone (FSH) receptor make it a suitable target for ovarian cancer. Here, we report a strategy to develop an organic near-infrared probe for FSH receptor-targeted tumor imaging and photothermal therapy. The FSH-Rh760 probe was conjugated from the Rh760 fluorophore with the FSH β subunit 33–53 peptide. FSH-Rh760 specifically distinguished peritoneal metastatic ovarian cancerous foci from surrounding normal tissues with a high tumor-to-background ratio. The fluorescence signals in tumors peaked at 2 h and were cleared at 120 h postinjection. FSH-Rh760 treatment rapidly increased the abdomen temperature of mice up to ~43 °C upon exposure to a near-infrared laser and effectively suppressed peritoneal tumor growth with tumor specificity. No significant systemic toxicities were observed. This study demonstrates the targeting ability and biocompatibility of FSH receptor-targeted theranostics and highlights its potential for clinical application in imaging-guided precision tumor resection and photothermal therapy to eliminate cancer lesions intraoperatively and postoperatively.

1. Introduction

Ovarian cancer remains the most lethal gynecologic malignancy [1]. More than 90 % of ovarian cancers are of epithelial origin and are often diagnosed at advanced stages with a 5-year survival rate of 20 %–40 %. First-line treatment consists of cytoreductive surgery and cisplatin-based combination chemotherapy. Even with a complete response to first-line treatment, most patients will experience relapse and drug resistance [2,3]. Although bevacizumab or poly ADP-ribose polymerase (PARP) inhibitors have shown therapeutic benefit, they have not significantly improved overall survival. The response rate of ovarian cancer to immunotherapy remains low, and some clinical trials have been terminated early due to a lack of efficacy [4,5]. Overall survival of advanced-stage ovarian cancer has not improved significantly despite advances in targeted therapy and immunotherapy.

Peritoneal dissemination is the predominant metastatic pattern of ovarian cancer, which differs from that of most epithelial malignancies. Shedding ovarian cancer cells form multicellular spheroids, invasively implant in the mesothelium and disseminate rapidly and widely in the peritoneal cavity [6]. This particular pattern of malignant progression makes cancerous foci difficult to effectively discern or easily ignored during surgery, resulting in residual or excessive resection. The R0 resection rate has been reported to be 8.1%–33.5 % in advanced ovarian cancer [7]. Moreover, the rate of optimal cytoreduction is often

* Corresponding author. Obstetrics and Gynecology Hospital of Fudan University, Shanghai, 200011, China.
** Corresponding author. Obstetrics and Gynecology Hospital of Fudan University, Shanghai 200011, China.
*** Corresponding author. Department of Chemistry, Fudan University, Shanghai 200438, China.
E-mail addresses: fyli@fudan.edu.cn (F. Li), zhxy@fudan.edu.cn (X. Zhang), xucongjian@fudan.edu.cn (C. Xu).
[1] These authors contributed equally to this work.

https://doi.org/10.1016/j.mtbio.2023.100904
Received 5 September 2023; Received in revised form 20 November 2023; Accepted 3 December 2023
Available online 7 December 2023

overestimated. Forty percent of patients who undergo optimal cytoreduction have residuals >1 cm on postoperative CT scans [8]. Patients with postoperative residuals are more likely to relapse, with a median survival of only 12–24 months after relapse [2]. Intraoperative imaging technology is needed to improve the cytoreductive surgery procedure to achieve complete resection of ovarian cancer.

In recent years, fluorescence image-guided surgery has developed rapidly. Long-wavelength probes such as near-infrared (NIR) fluorophores show translational potential due to their high resolution and high signal-to-noise ratio in the real-time detection of lesions during surgery [9,10]. However, NIR fluorophores are still not tumor specific, and it is difficult to distinguish cancerous from benign tissues in intraoperative settings. More efficient and specific targeted molecular imaging technology is needed for both surgeons and patients.

Furthermore, the peritoneal implantation and dissemination tropism of ovarian cancer makes some cancerous foci unresectable. Residual disease leads to relapse and poor prognosis in ovarian cancer patients. Adjuvant photothermal therapy can eliminate residual disease and further reduce tumor burdens [11]. Real-time evaluation of therapeutic efficacy is possible with precision imaging-guided photothermal therapy [12]. However, photothermal therapy may damage nontumor tissues due to the systemic biodistribution of photothermal agents. The selectivity of photothermal therapy can be improved by increasing the enrichment of photothermal agents at tumor sites [13,14].

Various drug delivery systems have been developed to increase drug accumulation in tumors via active or passive targeted strategies [15,16]. The tumor-specific recognition of imaging probes or therapeutic agents can be improved by targeting moieties that specifically bind to cell-surface biomarkers of cancer cells [9,17–19]. Follicle-stimulating hormone (FSH) receptor (FSHR) is expressed in ovarian cancer of different histologic types but not in other nonovarian healthy tissues [20,21]. The binding peptide domain from the FSH β chain shows high affinity for FSHR and has been used as a targeting moiety in peptide-based drug delivery platforms for ovarian cancer treatment [22–24]. FSHR could be a suitable target for molecular imaging or theranostic platforms in ovarian cancer.

Here, we report a strategy to develop an organic NIR tumor-targeting probe for intraoperative imaging and photothermal therapy of ovarian cancer. FSHR, which is expressed in ovarian cancer is used as the target for the theranostic probe. The theranostic probe FSH-Rh760 is conjugated from the Rh760 fluorophore with the FSH β subunit 33–53 peptide. The FSH β subunit 33–53 peptide, which has high affinity for FSHR, serves as the targeting moiety. The organic small molecule NIR fluorophore Rh760 serves as an imaging and photothermal agent due to its NIR fluorescence and photothermal properties. In a mouse model of peritoneal metastatic ovarian cancer, the FSH-Rh760 probe can specifically recognize and localize peritoneal metastatic foci and exhibits high accumulation in tumors with an optimal time window for imaging-guided surgery. Meanwhile, the FSH-Rh760 probe has efficient photothermal conversion properties and can effectively suppress peritoneal tumor growth by photothermal effects. This targeted theranostic probe exhibits specific tumor-targeting ability as well as good biocompatibility *in vivo*.

2. Materials and methods

2.1. Analysis of TCGA data

Transcriptome profiling data related to ovarian cancer samples were downloaded from the Cancer Genome Atlas (TCGA) data portal. The FSHR mRNA expression level was presented as fragments per kilobase of transcript per million mapped reads upper quartile (FPKM-UQ).

2.2. Cell culture

The human ovarian cancer cell lines A2780, IGROV-1 and SKOV-3 were used for the experiments. All cell lines were archived in our laboratory. Firefly luciferase and GFP gene-expressing A2780 cells (A2780-luciferase) were established by transducing lentiviral particles (Obio Technology, Shanghai, China). A2780, A2780-luciferase and IGROV-1 cells were cultured in RPMI-1640 medium containing 10 % fetal bovine serum (FBS). SKOV-3 cells were cultured in McCoy's 5A medium with 10 % fetal bovine serum.

2.3. Histology

A total of 134 human ovarian cancer samples were obtained from the Obstetrics and Gynecology Hospital of Fudan University. The procedure was approved by the Ethical Committee. Formalin-fixed paraffin-embedded tissue samples were sectioned at 5 μm thickness and then stained with standard hematoxylin-eosin (HE). For immunohistochemistry (IHC), the dewaxed tissue sections were incubated with the following primary antibodies: anti-FSHR (Cat# ab150557, Abcam, 1:100 dilution) and anti-cleaved caspase-3 (Cat# 9664, CST, 1:1000 dilution). For terminal deoxynucleotidyl transferase-mediated dUTP nick end labeling (TUNEL) assay, the dewaxed tissue sections were incubated with proteinase K solution and TUNEL reaction mixture according to the manufacturer's protocol of the *In Situ* Cell Death Detection Kit (Roche, Switzerland).

2.4. Western blotting

Protein lysates were obtained using RIPA buffer supplemented with protease inhibitor. Proteins were separated by 10 % SDS−PAGE and transferred to a nitrocellulose filter membrane (Millipore). The membranes were blocked and incubated with the following primary antibodies: anti-FSHR (Cat# ab75200, Abcam, 1:500 dilution) and anti-β-tubulin (Cat# abs830032, Absin, 1:1000 dilution). Proteins were visualized by chemiluminescence using the ImageQuant LAS 4000 system (GE Healthcare Life Sciences).

2.5. Synthesis of FSH-Rh760

Rh760 was synthesized according to previous work [25]. To couple with FSH peptides, Rh760-Paz and Rh760-GA were stepwise prepared from Rh760.

Synthesis of Rh760-Paz was performed as follows: Piperazine (3 mmol) and PyBOP (0.3 mmol) were added to a solution of Rh760 (0.3 mmol) in dry dichloromethane. The mixture was vigorously stirred at room temperature for 1 h, and the solvent was evaporated under reduced pressure. The residue was purified by a silica gel column using methanol:dichloromethane (v/v, 1:20) to collect compound Rh760-Paz as a dark green solid. The product was verified using ^{1}H nuclear magnetic resonance (NMR) and ^{13}C NMR spectroscopy (Bruker BioSpin International, Switzerland).

^{1}H NMR (400 MHz, DMSO-d_6, δ): 8.98 (s, 1H), 7.70–7.55 (m, 2H), 7.53 (d, J = 7.8 Hz, 1H), 7.35 (d, J = 7.8 Hz, 1H), 6.76 (dd, J_1 = 9.2 Hz, J_2 = 2.0 Hz,1H), 6.71 (d, J = 8.8 Hz, 1H), 6.26 (d, J = 2.0 Hz, 1H), 6.08 (d, J = 14.0 Hz, 1H), 3.46 (q, J = 6.8 Hz, 4H), 3.45–3.05 (m, 6H), 2.70–2.20 (m, 8H), 2.22 (m, 2H), 1.77–1.66 (m, 2H), 1.61 (s, 6H), 1.14 (t, J = 6.8 Hz, 6H).

^{13}C NMR (125 MHz, DMSO-d_6, δ): 178.04, 170.83, 167.20, 161.50, 155.34, 151.76, 147.71, 140.71, 135.55, 132.74, 131.18, 129.95, 129.32, 128.75, 127.86, 115.63, 114.68, 112.98, 112.06, 106.04, 96.50, 95.95, 46.34, 46.31, 45.01, 42.62, 26.54, 26.43, 26.36, 12.82.

Synthesis of Rh760-GA was performed as follows: Glutaric anhydride (0.5 mmol) was added to a solution of Rh760-Paz (0.3 mmol) in dry dichloromethane. The mixture was vigorously stirred at room temperature for 0.5 h, and the solvent was evaporated under reduced pressure. The residue was purified by a silica gel column using methanol: dichloromethane (v/v, 1:10) to afford compound Rh760-GA as a dark green solid. The product was verified using ^{1}H NMR and ^{13}C NMR

spectroscopy.

^{1}H NMR (400 MHz, DMSO-d_6, δ): 12.07 (s, 1H), 8.94 (s, 1H), 7.65–7.55 (m, 3H), 7.36 (d, $J = 7.2$ Hz, 1H), 6.75–6.65 (m, 2H), 6.60 (m, 1H), 6.08 (d, $J = 14.0$ Hz, 1H), 3.75–3.05 (m, 10H), 2.70–2.20 (m, 10H), 1.75–1.55 (m, 6H), 1.60 (s, 6H), 1.12 (t, $J = 7.0$ Hz, 6H).

^{13}C NMR (125 MHz, DMSO-d_6, δ): 178.01, 174.72, 174.58, 170.78, 167.42, 167.35, 161.48, 155.32, 151.75, 147.71, 135.75, 132.97, 130.24, 130.02, 129.30, 128.69, 127.84, 115.63, 114.67, 112.98, 112.11, 96.48, 95.93, 45.02, 33.37, 33.20, 31.84, 26.89, 26.55, 20.67, 20.55, 20.42, 12.67.

Synthesis of FSH-Rh760 was performed as follows: diisopropylamine (20 μL), HATU (0.05 mmol) and Rh760-GA (0.05 mmol) were added to 1 mL of dry DMF and allowed to react for 10 min under nitrogen protection. The FSH β subunit 33–53 peptide (YTRDLVYKDPARPKIQKTCTF) (5 mg) (Guoping Pharmaceutical, Hefei, China) was added to the solution and allowed to react for 2 h at room temperature. The mixture was evaporated under reduced pressure and subjected to high-performance liquid chromatography (HPLC) purification (Eluent: water/methanol) to obtain a green solid. The final product of FSH-Rh760 was identified by analytical HPLC and MALDI-TOF mass spectrometry. For FSH-Rh760: LRMS (MALDI-TOF) calcd [M+5H]5H+: 3292.82, found: 3292.50.

2.6. Photo-stability and chemical-stability of FSH-Rh760

FSH-Rh760, Rh760 and ICG in DMSO were irradiated continuously with an 808 nm laser (60 mW/cm^2) for 10 min. The photo-stability of the probe was determined by measuring the absorbance intensities. FSH-Rh760 was dissolved in RPMI-1640 medium containing 10 % FBS or H_2O for different time points. The chemical-stability of the probe was determined by measuring the time-dependent absorbance intensities at 785 nm.

2.7. Confocal fluorescence microscopy

To test the *in vitro* binding capacity of FSH-Rh760 and Rh760, A2780, IGROV1 and SKOV3 ovarian cancer cells were seeded in 8-well chamber slides (Ibidi) and grown to 50 %–60 % confluence. Cells were incubated with 10 μmol/L FSH-Rh760 or Rh760 for 90 min at 37 °C. After incubation, the cells were washed with PBS buffer, fixed in 4 % paraformaldehyde, labeled with WGA Alexa Fluor 488 conjugate (Invitrogen), and then sealed with mounting medium containing DAPI. The xenografts and major organs from the mouse model were sectioned into frozen slices of 7 μm thickness. Slides were fixed and mounted. These samples were analyzed using TCS SP5 confocal fluorescence microscopy (Leica).

2.8. Flow cytometry

Ovarian cancer cells were seeded into 6-well plates, grown to 60 %–70 % confluence, and incubated with 10 μmol/L FSH-Rh760 or Rh760 for 30 min at 37 °C. For the competition binding assay, cells were incubated with 2 μmol/L FSH-Rh760 and varying doses of FSH peptide (100 μmol/L or 200 μmol/L) for 30 min at 37 °C. Samples were measured using a CytoFLEX flow cytometer (Beckman Coulter). All experiments were performed in triplicate. Data were analyzed using FlowJo software (version 10.4).

2.9. Animal model

Female BALB/c nude mice (5 weeks old) were intraperitoneally injected with A2780 (1×10^7 cells), SKOV3 (5×10^6 cells) or A2780-luciferase (1×10^7 cells) ovarian cancer cells. Tumors were allowed to grow for 2–3 weeks before treatment. The studies were approved by the Institutional Animal Care and Use Committee of Fudan University.

2.10. NIR fluorescence imaging

FSH-Rh760 (3 mg/kg body weight) or Rh760 (0.52 mg/kg body weight) was intraperitoneally injected into nude mice with peritoneal metastatic xenografts of ovarian cancer. For *in vivo* competition binding experiments, the model mice were intraperitoneally coinjected with FSH-Rh760 (3 mg/kg body weight) and FSH peptide (22.8 mg/kg body weight). For *in vivo* imaging, mice were sacrificed at the indicated times from 0.5 h to 120 h postinjection (n = 3 per group), and the abdominal cavities were exposed. Fluorescence images were acquired using the IVIS Lumina K imaging system (PerkinElmer) with a 740 nm excitation filter and a 790 nm emission filter. For *ex vivo* imaging, tumors and major organs were immediately dissected and measured after sacrifice. Fluorescence signals were quantified as the average radiant efficiency ([p/s/cm^2/sr]/[μW/cm^2]) using the imaging system. The fluorescence intensity was measured by drawing a region of interest around the xenografts or mouse organs. The tumor-to-background ratio (TBR) was calculated as the average fluorescence intensity of the tumor divided by that of the skeletal muscle.

2.11. Bioluminescence imaging

Bioluminescence imaging in nude mice with peritoneal metastatic xenografts of A2780-luciferase ovarian cancer cells was performed using the IVIS Lumina K imaging system (PerkinElmer) 15 min after intraperitoneal injection of 150 mg/kg body weight d-luciferin (YEASEN Biotech, China). Bioluminescence signals were quantified as the total flux (p/s) of the entire abdomen.

2.12. In vivo photothermal therapy

To evaluate the photothermal properties, DMSO solutions of FSH-Rh760, Rh760 or ICG (1 mM) were illuminated with an NIR laser (808 nm, 60 mW/cm^2) for 5 min. Temperature changes were recorded using an infrared thermal camera (FLIR E40).

For *in vivo* photothermal therapeutic experiments, nude mice with peritoneal metastatic xenografts of A2780-luciferase ovarian cancer cells were randomly divided into six groups (n = 5 per group). Three groups received NIR laser irradiation after intraperitoneal injection with FSH-Rh760 (6 mg/kg body weight), Rh760 (1.04 mg/kg body weight) or PBS. The other three groups were only injected with the same dose of FSH-Rh760, Rh760 or PBS. Mice were anesthetized at 2 h postinjection, and the whole abdomen was exposed to an 808 nm laser (60 mW/cm^2) for 10 min. Temperature changes were recorded during laser irradiation using an infrared thermal camera. Photothermal therapy started on the 7th day after tumor implantation and was conducted every 3 days 4 times. Tumor burden was measured twice a week via bioluminescence imaging. Changes in body weight were recorded every 3 days. After 2 weeks of treatment, the mice were sacrificed and dissected to inspect the peritoneal tumor foci and major organs. Peritoneal tumor nodules with a diameter of $\geq$2 mm were excised and counted. The tissue sections were histologically examined as described earlier.

2.13. In vivo toxicity test

The systemic toxicity of FSH-Rh760 was determined in BALB/c nude mice. Mice were intraperitoneally injected with FSH-Rh760 (3 mg/kg body weight), Rh760 (0.52 mg/kg body weight) or vehicle and were followed for 6 days (n = 4 per group). Mouse body weights were recorded every other day. Blood draws were performed to assess white blood cells (WBCs), red blood cells (RBCs), platelets (PLTs), alanine transaminase (ALT), aspartate transaminase (AST), blood urea nitrogen (BUN) and creatinine (CREA). Heart, lung, liver, spleen, kidney and ovary tissues were harvested for HE staining and histopathological examination. Additionally, tissues of major organs were subjected to HE staining after photothermal therapy to evaluate the potential toxicity of

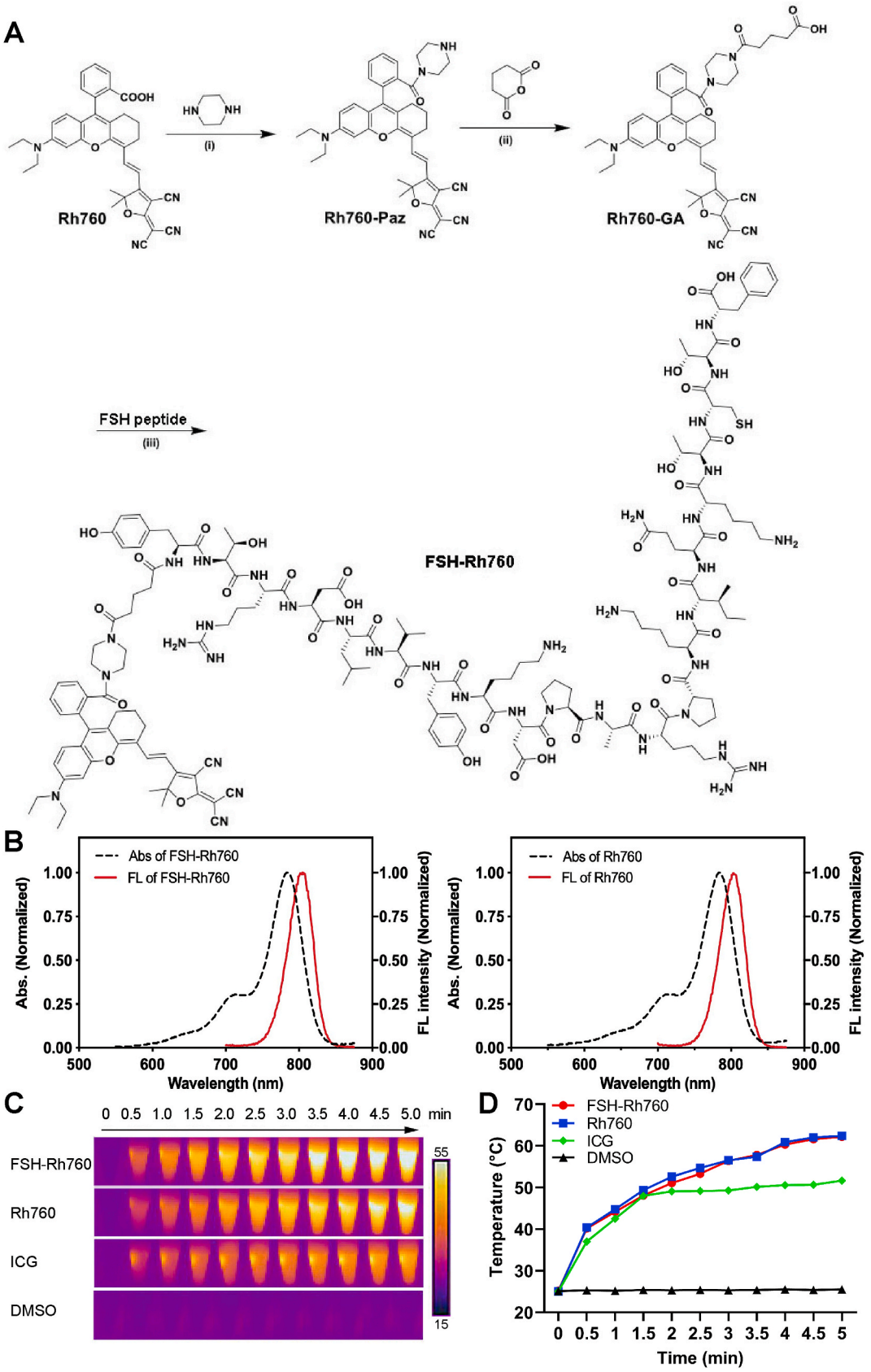

Fig. 1. Synthesis and characterization of FSH-Rh760. A, Synthetic scheme of FSH-Rh760. **B,** UV–Vis absorbance and fluorescence spectra of FSH-Rh760 and Rh760. **C** and **D,** Photothermal images and temperature-rising curves of FSH-Rh760, Rh760 and ICG in DMSO solutions under NIR irradiation (808 nm, 60 mW/cm^2) for 5 min.

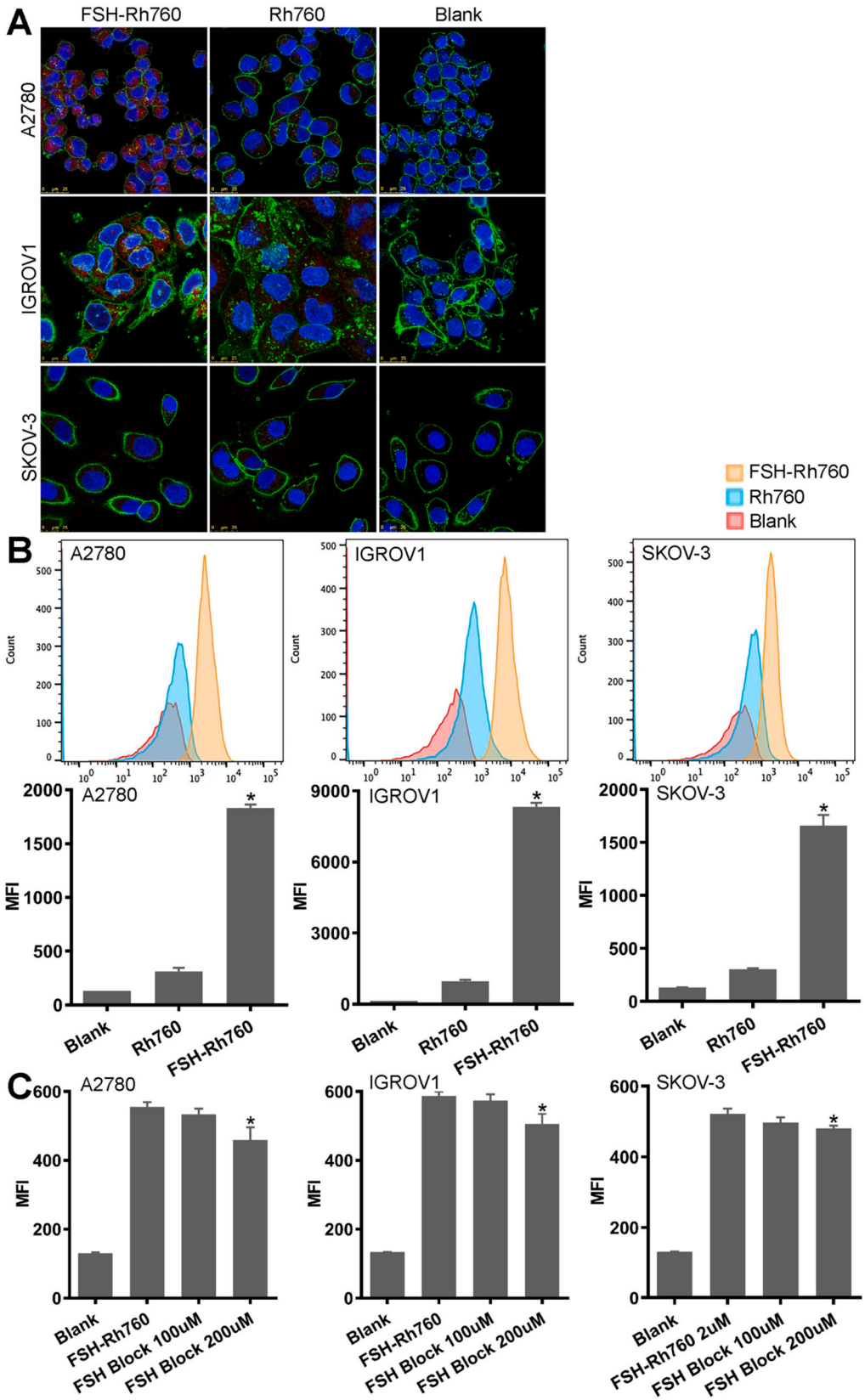

Fig. 2. Cell binding capacity of FSH-Rh760. A, Confocal fluorescence microscopy images of ovarian cancer cells. Cells were incubated with 10 μmol/L FSH-Rh760 or Rh760 for 90 min at 37 °C. The cell membrane was labeled with WGA Alexa Fluor 488 conjugate (green), the nucleus was labeled with DAPI (blue), and the fluorescence signal was presented by FSH-Rh760 or Rh760 (red). Bar, 25 μm. **B,** Flow cytometry of ovarian cancer cells. Cells were incubated with 10 μmol/L FSH-Rh760 or Rh760 for 30 min at 37 °C. **C,** Competition binding assay via flow cytometry. Cells were incubated with 2 μmol/L FSH-Rh760 and 100 μmol/L or 200 μmol/L FSH peptide for 30 min at 37 °C. The mean fluorescence intensity (MFI) values were compared between the FSH-Rh760 and Rh760 incubation groups (n = 3). $^{*}P < 0.05$. (For interpretation of the references to colour in this figure legend, the reader is referred to the Web version of this article.)

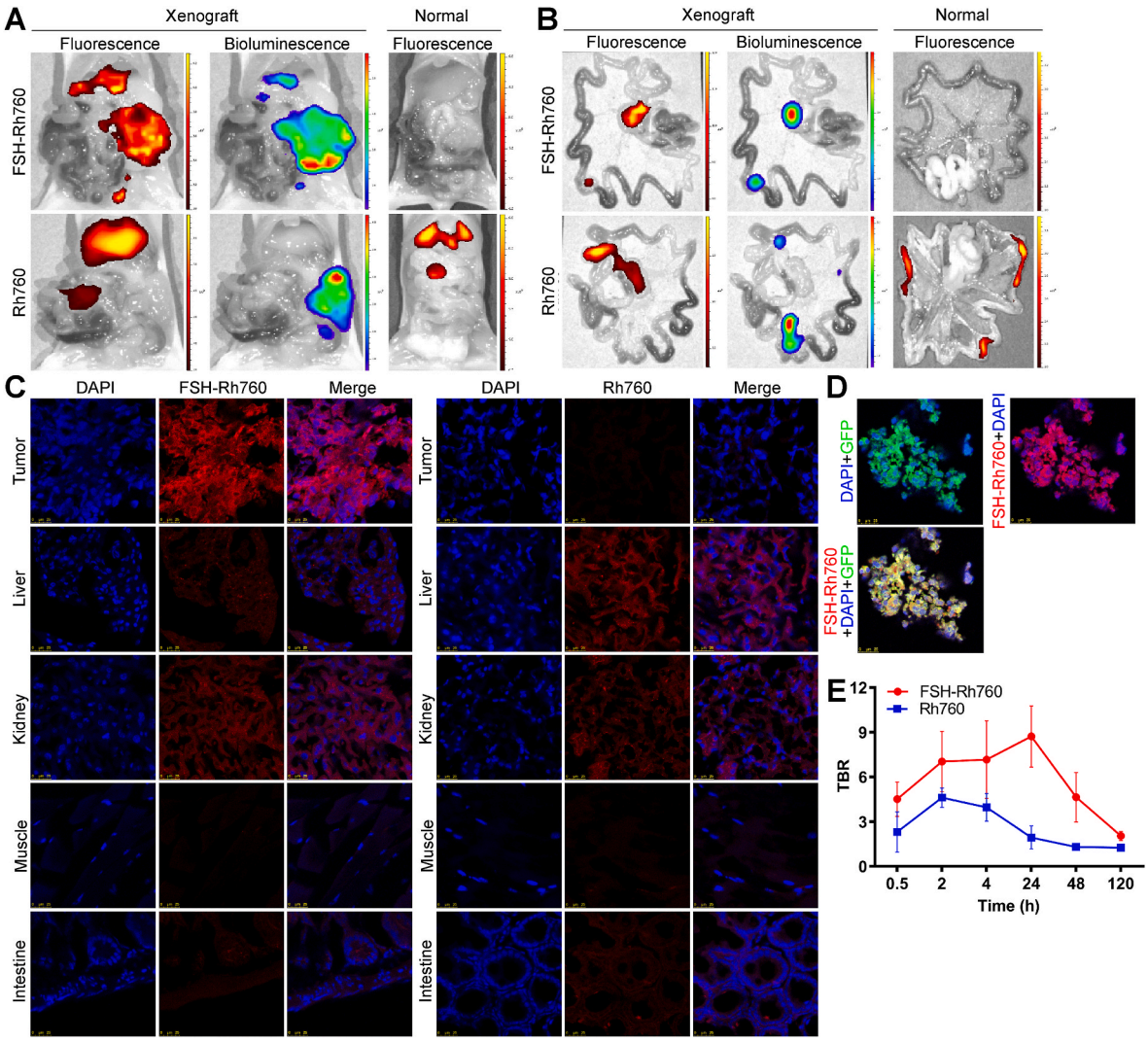

Fig. 3. FSH-Rh760 localized to FSHR-positive peritoneal ovarian cancer. FSH-Rh760 or Rh760 was intraperitoneally injected into nude mice with peritoneal metastatic xenografts of A2780-luciferase ovarian cancer cells and normal nude mice without xenografts. Fluorescence imaging was performed at the indicated times. Bioluminescence imaging was performed 15 min after intraperitoneal injection of d-luciferin. **A** and **B,** Fluorescence and bioluminescence imaging of the peritoneal cavity *in vivo* and the intestine *ex vivo* at 2 h postinjection of the probes. **C,** Confocal fluorescence microscopy images of frozen tissue sections of tumors and major organs in mice with A2780-luciferase xenografts. Bar, 25 μm. **D,** The colocalization of GFP signals from A2780-luciferase ovarian cancer cells (green) and signals from FSH-Rh760 (red). Nuclei were labeled with DAPI (blue). Bar, 25 μm. **E,** TBR of FSH-Rh760 and Rh760 from 0.5 h to 120 h postinjection (n = 3). (For interpretation of the references to colour in this figure legend, the reader is referred to the Web version of this article.)

laser irradiation.

2.14. Statistical analysis

The unpaired Student's *t*-test was used for comparisons between two variables. All data are presented as mean ± standard deviation. Values of $P < 0.05$ were considered statistically significant. Statistical analysis was performed using the GraphPad Prism software (version 8).

3. Results

3.1. FSHR expression in ovarian cancer

We first analyzed 227 cases of serous ovarian cancer from TCGA datasets. The expression of FSHR mRNA was found in 60.9 % of these samples (Supplementary Fig. S1A). FSHR protein expression was examined in 134 ovarian cancer tissue samples of multiple histologic types, with 73.1 % of these samples expressing FSHR (Supplementary Table S1, Supplementary Fig. S1B). Positive staining was found in 72.8 % of serous carcinomas and 58.3 % of mucinous carcinomas. FSHR expression was also found in endometrioid and clear cell ovarian cancer. FSHR expression in ovarian cancer cell lines was evaluated by western blotting. The A2780 and IGROV-1 cell lines showed high expression levels and were used as positive controls; the SKOV-3 cell line showed low expression levels and was used as a negative control for subsequent experiments (Supplementary Fig. S1C). In addition, we analyzed FSHR expression in normal tissues from the Genotype-Tissue Expression (GTEx) Portal database. FSHR has limited expression in other healthy tissues and is primarily expressed in the ovaries of females (Supplementary Fig. S2). Collectively, these data suggest that FSHR could be a potential target for molecular imaging and the development of therapeutics for ovarian cancer.

3.2. Synthesis and characterization of FSH-Rh760

The NIR dye Rh760 was synthesized as previously reported [25]. Rh760-Paz and Rh760-GA were stepwise prepared from Rh760, and then the FSH β subunit 33–53 peptide was conjugated to Rh760-GA to

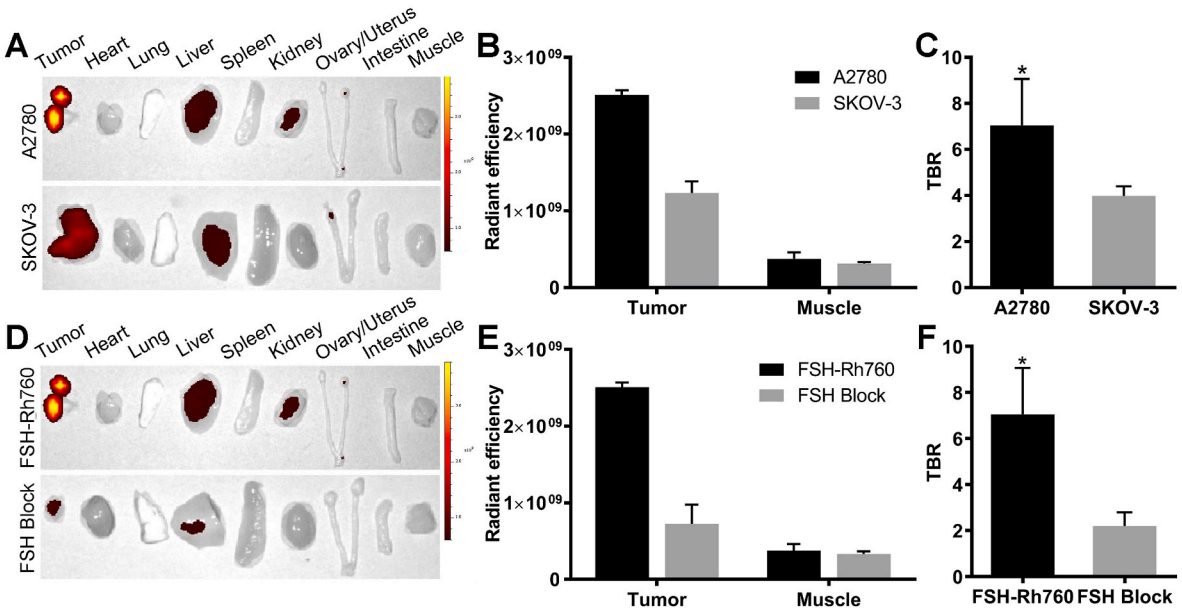

Fig. 4. Specific tumor binding of FSH-Rh760. A-C, Fluorescence imaging of tumors and major organs *ex vivo*, radiant efficiency of tumor and background muscle tissues, and TBR from nude mice with peritoneal metastatic xenografts of A2780 and SKOV-3 ovarian cancer cells after intraperitoneal injection of FSH-Rh760 (n = 3). **D-F,** Fluorescence imaging of tumors and major organs *ex vivo*, radiant efficiency of tumor and background muscle tissues, and TBR from nude mice with peritoneal metastatic xenografts of A2780 ovarian cancer cells after intraperitoneal coinjection of FSH-Rh760 and FSH peptide (n = 3). Fluorescence imaging was performed at 2 h postinjection. $^{*}P < 0.05$.

assemble the final targeted probe FSH-Rh760 (Fig. 1A). Rh760-Paz and Rh760-GA were verified using ^{1}H NMR and ^{13}C NMR spectroscopy (Supplementary Fig. S3-S4). FSH-Rh760 was identified by analytical HPLC and MALDI-TOF mass spectrometry (Supplementary Fig. S5). The molecular weight of FSH-Rh760 was 3292.50 Da. The purity of FSH-Rh760 was 95.48 %. In DMSO solution, FSH-Rh760 had an excitation wavelength of 785 nm and an emission wavelength of 805 nm, which was similar to the Rh760 dye (Fig. 1B). The FSH-Rh760 probe showed better photo-stability than the clinically approved ICG probe under 808 nm laser excitation (Supplementary Fig. S6A). The absorbance of FSH-Rh760 was stable in different solutions (Supplementary Fig. S6B-C), indicating the chemical-stability of the probe.

The photothermal property of FSH-Rh760 was further investigated. After NIR laser irradiation (60 mW/cm^2) for 5 min, the maximum increased temperature (ΔT_{max}) of FSH-Rh760 and Rh760 was ~37 °C, whereas the ΔT_{max} of indocyanine green (ICG) and DMSO was ~26 °C and ~0.5 °C, respectively (Fig. 1C–D). FSH-Rh760 and Rh760 exhibited highly efficient photothermal conversion properties and could be promising theranostic agents.

3.3. The enhanced cell binding capacity of FSH-Rh760

To test the cell targeting capacity, we incubated FSH-Rh760 and Rh760 with ovarian cancer cell lines with different FSHR expression levels. The FSHR-positive cell lines (A2780 and IGROV1) treated with FSH-Rh760 presented higher fluorescence signals than the control SKOV3 cells (Fig. 2A). The naked Rh760 dye showed a weaker fluorescence signal than FSH-Rh760 in A2780 and IGROV1 cells. We further evaluated the accumulation of FSH-Rh760 in ovarian cancer cells by flow cytometry. A significant difference in mean fluorescence intensity was observed between FSH-Rh760 and Rh760 in FSHR-positive ovarian cancer cells (Fig. 2B). The uptake of FSH-Rh760 in ovarian cancer cells was competitively inhibited by FSH β subunit 33–53 peptides (Fig. 2C). These data demonstrated the FSHR-specific binding capacity of FSH-Rh760 in ovarian cancer cells.

3.4. FSH-Rh760 specifically recognized peritoneal metastases of ovarian cancer

The *in vivo* imaging property of FSH-Rh760 was evaluated using a nude mouse model with peritoneal metastatic xenografts of A2780 or A2780-luciferase ovarian cancer cells. Fluorescence or bioluminescence imaging was performed at the indicated times after intraperitoneal injection of FSH-Rh760 or Rh760 using the IVIS Lumina K imaging system. Based on the dose-escalation study, a dose of 3 mg/kg body weight was used for the following experiments because of the higher TBR (Supplementary Fig. S7). At 2 h postinjection of the probes, the localization of fluorescence signals from FSH-Rh760 was consistent with the tumor border defined by bioluminescence imaging in mice with A2780-luciferase xenografts (Fig. 3A). In contrast, the accumulation of Rh760 was mainly observed in the liver. Normal control mice injected with FSH-Rh760 showed few fluorescence signals, which indicated a low background in normal tissues. The corresponding *ex vivo* imaging of the intestine with mesenteric metastases is shown in Fig. 3B. Tiny metastatic nodules on the mesentery were also recognized, while the intestine had few fluorescence signals in the FSH-Rh760 group. Consistently, confocal fluorescence imaging of frozen tissue sections from *ex vivo* tumors and major organs confirmed the accumulation of FSH-Rh760 in tumors, while Rh760 showed strong fluorescence signals in liver tissue (Fig. 3C). The tumor binding of FSH-Rh760 was further demonstrated by colocalization of GFP signals from A2780-luciferase ovarian cancer cells and signals from the FSH-Rh760 probe (Fig. 3D).

To further evaluate the capacity of FSH-Rh760 to distinguish peritoneal metastases from background tissues, the TBR was calculated at the indicated time points from 0.5 h to 120 h (Fig. 3E). The maximal TBR of FSH-Rh760 was 8.73 ± 2.06 at 24 h postinjection, which was 4.45-fold higher than that of Rh760 (1.96 ± 0.77). The TBR of FSH-Rh760 maintained a high level during the investigated period from 2 h to 48 h. Additionally, FSH-Rh760 exhibited stronger fluorescence signals and higher TBR in A2780 xenografts (FSHR-positive) than in SKOV-3 xenografts with low FSHR expression (Fig. 4A–C). Coinjection of FSH peptide with FSH-Rh760 significantly suppressed the tumor binding of FSH-Rh760 in nude mice with A2780 xenografts (Fig. 4D–F). Taken

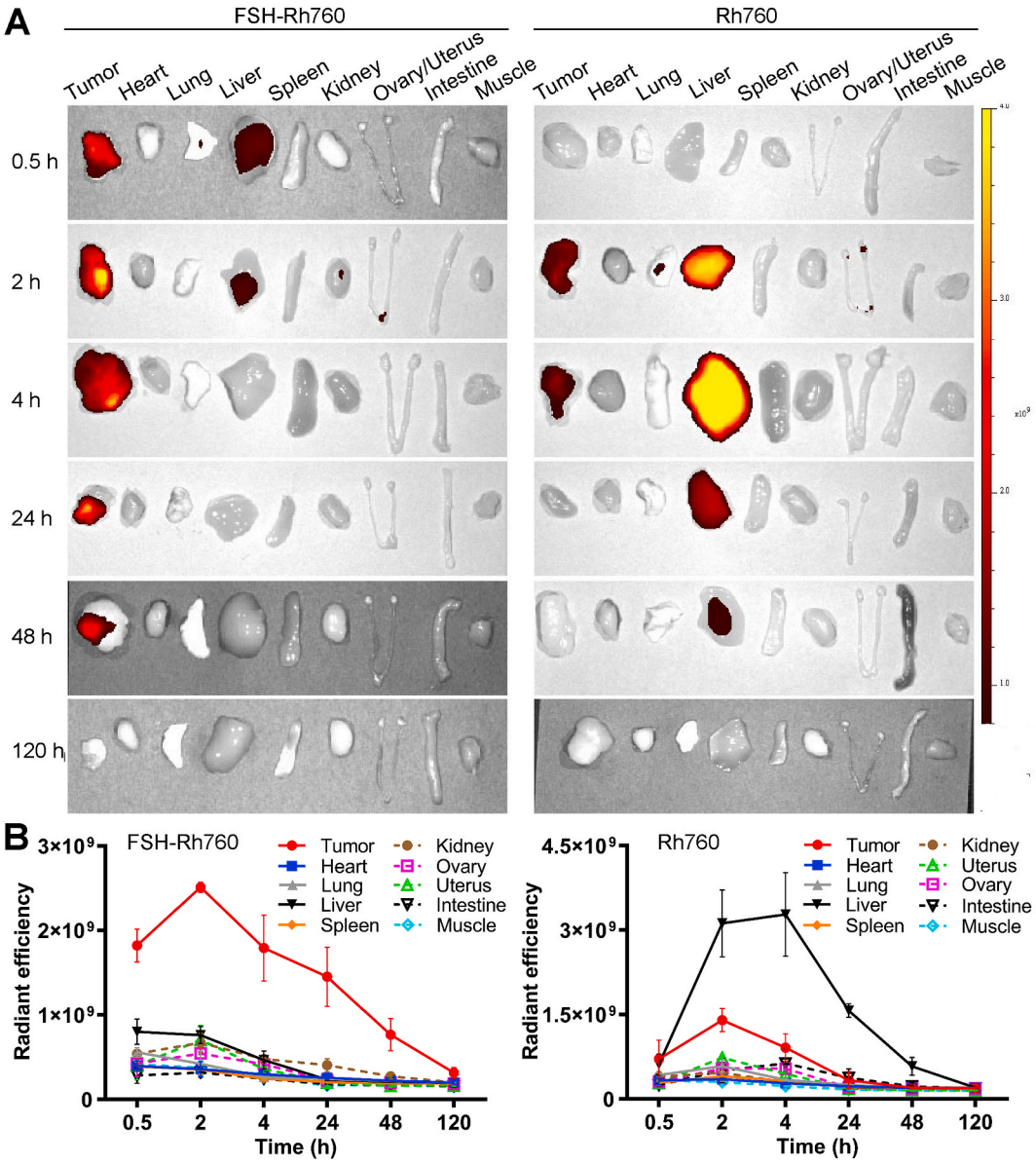

Fig. 5. ***In vivo*** **systemic biodistribution and kinetics of FSH-Rh760 and Rh760.** FSH-Rh760 or Rh760 was intraperitoneally injected into nude mice with peritoneal metastatic xenografts of A2780 ovarian cancer cells. Fluorescence imaging was performed from 0.5 h to 120 h postinjection. **A,** Fluorescence imaging of tumors and major organs *ex vivo*. **B,** Changes in the fluorescence intensity in tumors and major organs (n = 3).

together, these data suggested that FSH-Rh760 could specifically recognize and localize to peritoneal metastatic foci without acting on normal tissues and intestinal tissues.

3.5. *In vivo systemic biodistribution of FSH-Rh760*

The biodistribution and kinetics of FSH-Rh760 and Rh760 were further evaluated using a nude mouse model with peritoneal metastatic xenografts of A2780 ovarian cancer cells. Fluorescence imaging was performed from 0.5 h to 120 h after intraperitoneal injection of FSH-Rh760 or Rh760. Representative *ex vivo* fluorescence images of tumors and major organs at different time points are presented in Fig. 5A. The changes in mean fluorescence intensities were analyzed (Fig. 5B). The accumulation of FSH-Rh760 in A2780 tumors occurred in a time-dependent manner with a high level from 0.5 h to 48 h postinjection. The fluorescence signals in tumors peaked at 2 h postinjection and were then cleared at 120 h postinjection. Low levels of fluorescence signals were observed in the liver and kidney, which disappeared at 24 h and 120 h postinjection, respectively. Few fluorescence signals were detected in the intestine and other normal tissues. In comparison, Rh760 continuously exhibited the highest fluorescence signals in the liver when compared to all other tissues. Although slight fluorescence signals were observed in tumors because of the enhanced permeability and retention effect, the fluorescence signals decreased quickly postinjection. These data indicated a high accumulation of FSH-Rh760 in tumors and an optimal time window for imaging-guided surgery.

3.6. *In vivo photothermal therapeutic effect of FSH-Rh760 on peritoneal metastases of ovarian cancer*

Based on the *in vivo* biodistribution and photothermal properties of FSH-Rh760, the photothermal therapeutic effect of FSH-Rh760 on ovarian cancer was further evaluated. The study schema is shown in Fig. 6A. Nude mice bearing peritoneal metastatic xenografts of A2780-luciferase ovarian cancer cells were exposed to NIR light (808 nm, 60 mW/cm^2) for 10 min at 2 h post FSH-Rh760, Rh760 or PBS injection.

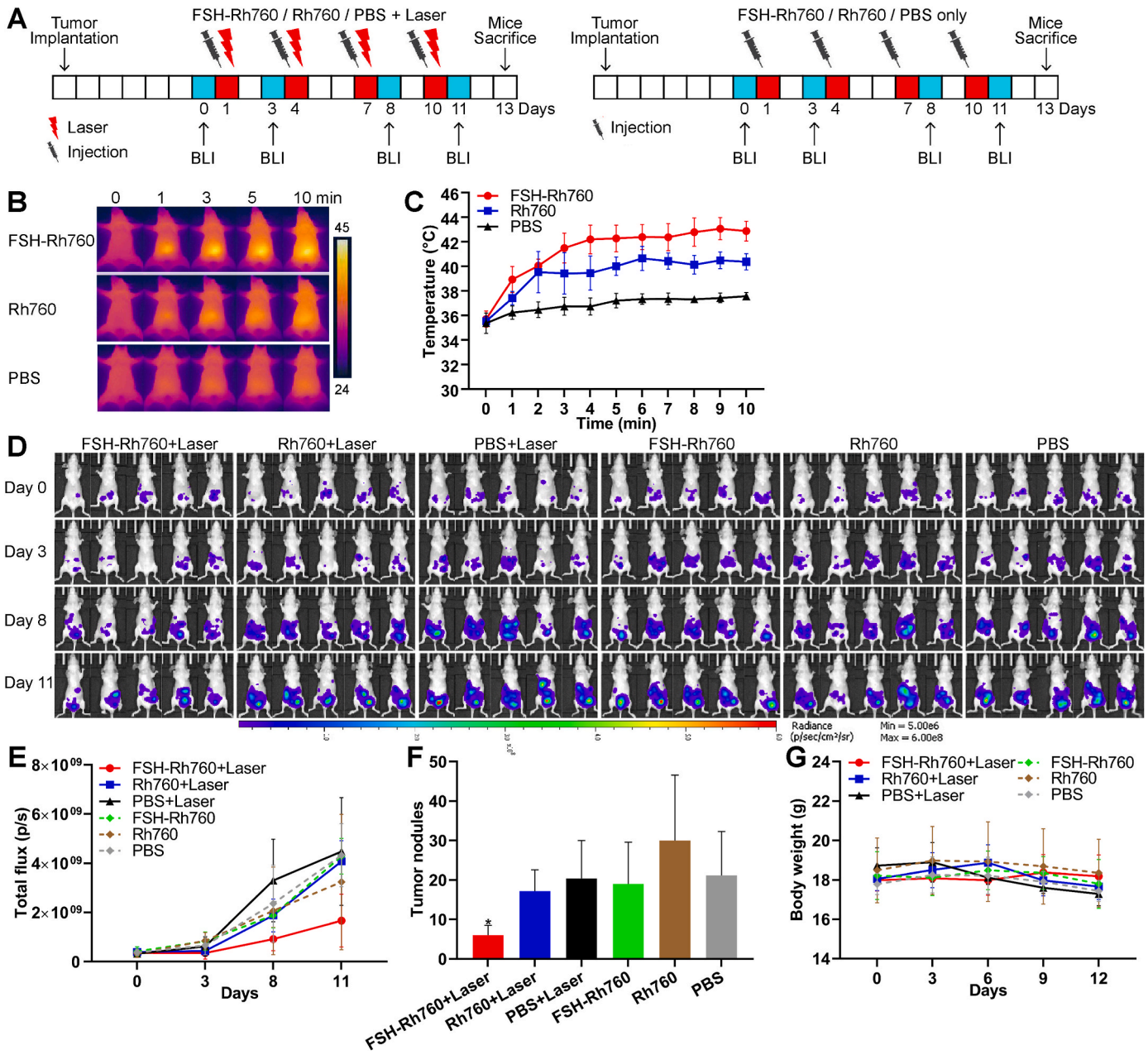

Fig. 6. ***In vivo*** **photothermal therapeutic effect of FSH-Rh760 on peritoneal metastases of ovarian cancer. A,** The study schema of *in vivo* photothermal therapy. Nude mice with peritoneal metastatic xenografts of A2780-luciferase ovarian cancer cells were divided into six groups. Three groups received NIR laser irradiation after intraperitoneal injection with FSH-Rh760, Rh760 or PBS. The other three groups only received FSH-Rh760, Rh760 or PBS. Photothermal therapy was conducted every 3 days 4 times. Tumor burden was measured twice a week via bioluminescence imaging (BLI). **B,** Representative infrared thermal images of mice exposed to the NIR laser. **C,** Temperature-rising curves of the mouse abdomen after NIR laser exposure. **D,** *In vivo* bioluminescence images of mice bearing A2780-luciferase xenografts. **E,** Changes in the bioluminescence intensities of A2780-luciferase xenografts. **F,** The number of peritoneal tumor nodules at the end point. **G,** Changes in mouse body weight. $^{*}P < 0.05$.

The corresponding groups without NIR laser irradiation were also used as controls. As shown in Fig. 6B–C, FSH-Rh760 treatment rapidly increased the abdomen temperature of mice up to ~43 °C upon exposure to NIR light. Compared to Rh760, higher tumor accumulation of FSH-Rh760 could generate better photothermal conversion under laser exposure. The PBS-treated control group exhibited a slight temperature increase with a maximum temperature of 37.5 °C.

The antitumor effect was evaluated via the dynamic changes in the bioluminescence intensities of A2780-luciferase xenografts and the number of peritoneal tumor nodules at the end point. As shown in the bioluminescence imaging, tumor growth was significantly suppressed in mice that received FSH-Rh760 with NIR laser irradiation (Fig. 6D–E). In contrast, tumor growth was not affected by FSH-Rh760 treatment alone, Rh760 treatment with or without NIR laser irradiation or NIR laser irradiation alone. Their tumor growth rates were similar to those of the nontreated PBS control group. The bioluminescence imaging data were consistent with the counting data of peritoneal tumor nodules at the end point. The mice that received FSH-Rh760 with NIR laser irradiation exhibited the fewest peritoneal tumor nodules with a value of 6.0 ± 2.5 among all groups (Fig. 6F). Additionally, the body weights of the mice had no obvious fluctuations during treatment (Fig. 6G). HE staining of the major organs of mice showed no obvious abnormalities (Supplementary Fig. S8).

To further evaluate the hyperthermia effects of FSH-Rh760 on

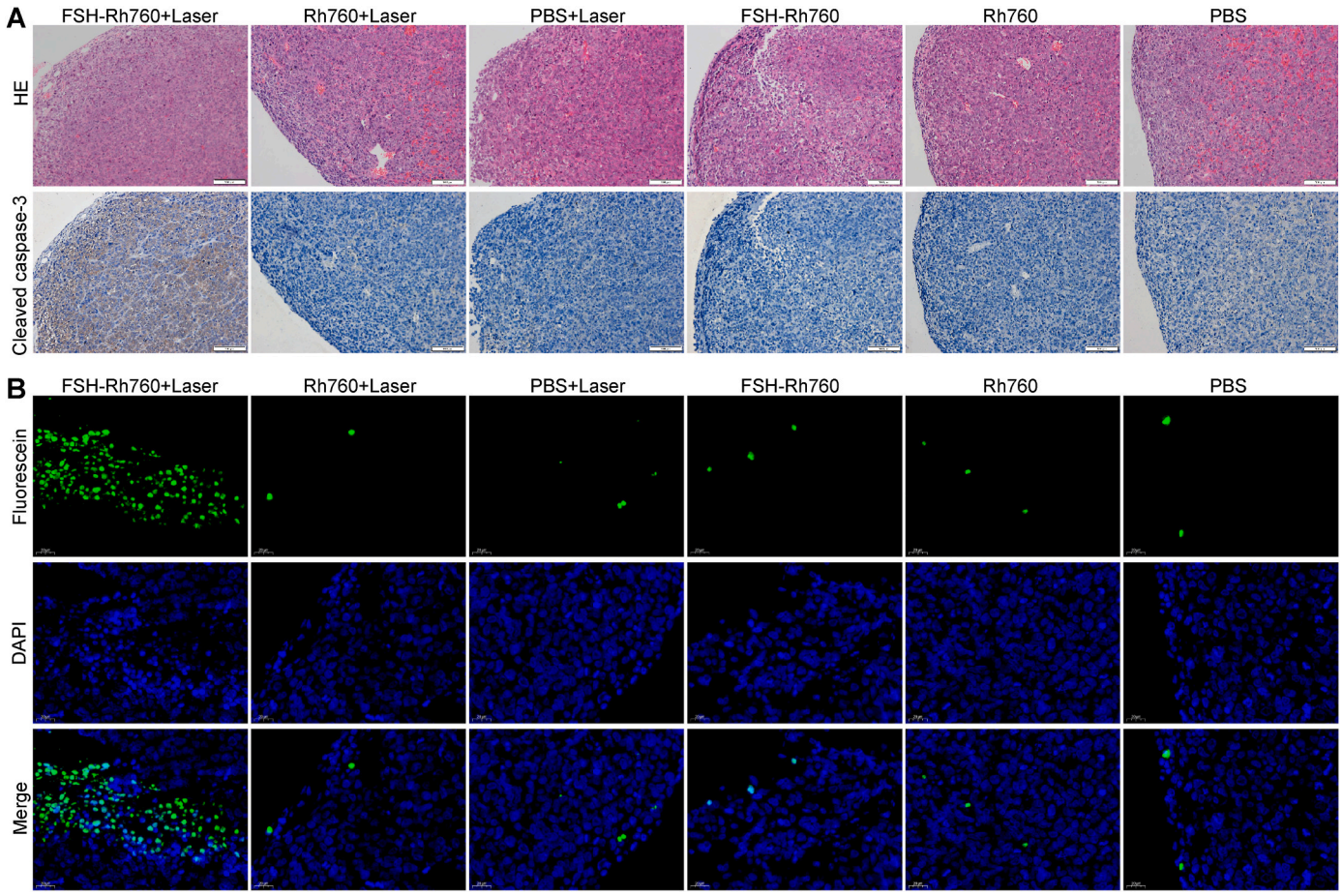

Fig. 7. Histopathological analyses of xenografts from photothermal-treated mice. At the end point of photothermal therapy, the mice were sacrificed, and xenografts were collected. **A,** HE staining and IHC staining of cleaved caspase-3 in xenografts. Bar, 100 μm. **B,** TUNEL staining of xenografts. Bar, 20 μm.

ovarian cancer, the apoptosis of cancer cells in xenografts was analyzed at the end point of photothermal therapy. As shown in Fig. 7A, cleaved caspase-3 expression was increased in the FSH-Rh760 group with laser irradiation treatment. TUNEL staining also revealed many apoptotic cancer cells in this group (Fig. 7B). Taken together, these results show that FSH-Rh760-based photothermal therapy was effective in suppressing FSHR-positive peritoneal tumor growth with minimal toxicity.

3.7. *In vivo* toxicity of FSH-Rh760

The systemic toxicity of FSH-Rh760 and Rh760 was further determined in BALB/c nude mice by measurement of body weight, blood cells, liver and renal function and histopathology of major organs (Fig. 8). No significant difference was observed in body weights during the treatment period. The levels of WBCs, RBCs, PLTs, ALT, AST, BUN and CREA were not significantly different between the FSH-Rh760 and control groups on the 6th day posttreatment. A slight decrease in ALT level was observed in the Rh760-treated group, but the level remained within the normal reference range. Histopathological examination of the heart, lung, liver, spleen, kidney and ovary did not present any obvious damage, which further confirmed the *in vivo* biocompatibility of FSH-Rh760.

4. Discussion

The tumor-targeting ability and biocompatibility of theranostic platforms are still challenging for their clinical translation in ovarian cancer. To provide new approaches for improving the effectiveness and minimizing the toxicity of theranostic platforms, we conjugated the FSH β subunit 33–53 peptide to the organic NIR fluorophore Rh760 to develop a tumor-targeting theranostic agent for ovarian cancer. The FSH β subunit 33–53 amino acids show a high affinity to FSHR, which has a large extracellular domain containing the recognition and binding sites with its ligand FSH [26–28]. Although the location of FSHR is the granulosa cells of the ovary in females rather than other nongonad tissues, FSHR expression has been reported in ovarian cancer of different histologic types, ranging from 50 % to 84 % [20,29–31]. We reported an FSHR-positive expression rate of 73.1 % in ovarian cancer tissues, consistent with previous reports. Moreover, FSHR is highly expressed in endothelial cells of tumor tissues but is not expressed in normal tissues located more than 10 mm from tumors [21]. The expression patterns of FSHR, including its location at the boundary between cancerous foci and normal tissues, low expression level in gonadal endothelial cells, and negative expression in nonovarian healthy tissues, make it useful for tumor-targeting imaging and therapy with minimal toxicity [20–22,32].

FSHR on the luminal endothelial surface of tumor xenografts can bind and deliver its ligands [21]. The peptide sequences derived from the binding domains of FSH have been employed as targeting ligands to ovarian cancer in drug delivery systems, aiming to specifically target cancerous foci without damaging healthy tissues [22–24,28,33]. The specific recognition and binding of the FSH-Rh760 probe to ovarian cancer were evaluated *in vitro*, *in vivo* and *ex vivo* in this study. Significantly higher fluorescence signals were observed in FSHR-positive ovarian cancer cells and xenografts from the FSH-Rh760-treated mouse model compared to the group treated with Rh760. The colocalization of fluorescence signals from FSH-Rh760 probes, bioluminescence signals and GFP staining from xenografts of A2780-luciferase cells indicated the selective binding and uptake of FSH-Rh760 probes by

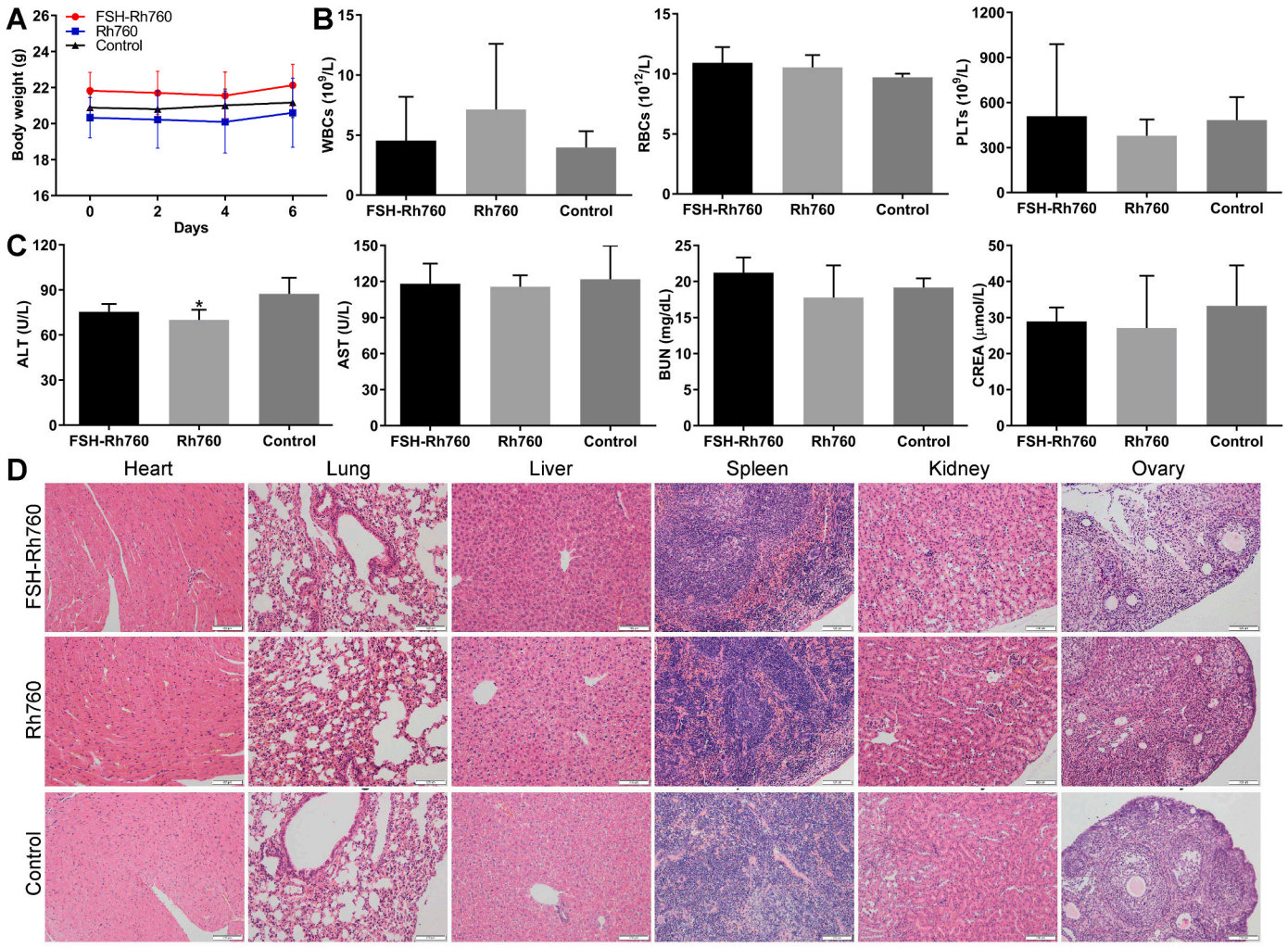

Fig. 8. ***In vivo*** **toxicity of FSH-Rh760 and Rh760.** BALB/c nude mice were intraperitoneally injected with FSH-Rh760, Rh760 or vehicle and were followed for 6 days. **A,** Changes in the body weight of mice. **B,** The levels of blood cells at the end point. **C,** Liver and renal function at the end point. $^*P < 0.05$. **D,** HE staining of major organs. Bar, 100 μm.

FSHR-positive ovarian cancer cells. The uptake of FSH-Rh760 by ovarian cancer cells was competitively inhibited by FSH β subunit 33–53 peptides, which further proved the FSHR-specific binding capacity of FSH-Rh760. The targeting ability of FSH-Rh760 probes to ovarian cancer allows specific tumor imaging and imaging-guided surgery.

Intraoperative tumor-targeted imaging is particularly important in ovarian cancer, which has a peritoneal dissemination tropism with common metastatic sites of mesentery and intestine tissues. This particular metastatic pattern makes tumor foci difficult to discern, affecting surgical completeness and postoperative morbidity. Fluorescence image-guided surgery with tumor-targeting by means of folate receptor, HER2, prolactin receptor, CD24 or other biomarkers has shown the potential to improve the detection and resection of tumor foci in ovarian cancer [9,17,18,34–38]. Visible, first-window or second-window NIR real-time imaging systems have been developed in preclinical and clinical settings. NIR imaging-guided surgery can ensure precise resection by providing accurate tumor margin imaging during the operation [39].

Here, FSHR was used as the target for specific tumor imaging due to its high expression in different histologic types of ovarian cancer as well as its negative expression in the surrounding nonovarian healthy tissues. The first-window NIR organic fluorophore Rh760 served as an imaging agent based on its good modifiability, high luminescence efficiency and biocompatibility [25]. Peritoneal ovarian cancer xenografts were built to better mimic the clinical metastatic patterns of advanced ovarian cancer, supporting their application in intraoperative settings. The probes were intraperitoneally administered, which might weaken uptake in the liver and reduce potential toxicity compared to systemic intravenous administration [40,41]. *In vivo* and *ex vivo* imaging data revealed that the FSH-Rh760 probe could specifically localize and be used to image peritoneal tumors from the surrounding mesentery and intestine tissues in comparison to Rh760. Modification with FSH peptides changed the systemic biodistribution pattern of Rh760 dye, enabling it to specifically accumulate in tumors at a high level from 0.5 h to 48 h postinjection. The accumulation period provides an optimal time window for imaging-guided surgery. In contrast, little accumulation of Rh760 was observed in tumors and the amount of accumulated Rh760 declined quickly.

Although optimal cytoreduction is defined as no more than 1 cm of macroscopically visible residuals, patients with R0 resection have a better prognosis [42]. In addition to improving the resection rate with the aid of intraoperative targeted imaging, photothermal therapy can serve as an adjuvant to surgery with the advantages of noninvasiveness, deep penetration, and minimal damage to normal tissues [11,43]. Here, both Rh760 and FSH-Rh760 exhibited more efficient photothermal conversion properties than ICG. High accumulation of FSH-Rh760 at tumor sites generated good photothermal effects, leading to suppression of peritoneal tumor growth and induction of tumor cell apoptosis.

FSH-Rh760 treatment rapidly increased the abdomen temperature of mice up to 43 °C upon exposure to NIR light. This degree of mild temperature hyperthermia can induce cell death by activating the apoptotic response in a more regulated manner in contrast to high (45 °C) hyperthermia [44]. Mild (43 °C) hyperthermia activates extrinsic and intrinsic apoptotic pathways as well as ER stress sensors [44]. Our data also proved that apoptosis was induced by FSH-Rh760 photothermal treatment in ovarian cancer. Interestingly, hyperthermia can induce tumor-associated antigen release and immunogenic cell death, leading to the synergistic enhancement of the antitumor effects of immune checkpoint inhibitors [45–49]. Some functionalized nanomaterials show immunoregulatory effects and anticancer capacity via reactive oxygen species in the local microenvironment [50,51]. However, the modulating effects on the tumor immune microenvironment of FSH-Rh760 photothermal treatment were not examined in the current study because immunodeficient mice with peritoneal xenografts were used. Furthermore, the tissue penetration depth and thermal resistance of photothermal therapy need to be investigated before clinical application. The combination of photothermal therapy with a heat shock protein blocking strategy might be a promising approach to overcome thermal tolerance [52].

The safety of imaging probes and photothermal therapy remains a concern for their clinical application. No significant toxicity was detected following a six-day exposure to the FSH-Rh760 probe through measurements of blood panels and histopathology of major organs. At the end of photothermal treatment with FSH-Rh760, no visible damage to major organs was observed. However, further assessments are required following prolonged exposure to the probe.

5. Conclusion

In conclusion, we demonstrated the targeting ability and biocompatibility of an FSH peptide-conjugated NIR probe to identify peritoneal metastatic foci and revealed its photothermal therapeutic effects on peritoneal metastases in ovarian cancer. These findings highlight the potential of FSHR-targeted theranostics for clinical application in imaging-guided precision tumor resection and photothermal therapy to eliminate cancer lesions intraoperatively and postoperatively. Further evaluation in clinical settings is required before clinical application.

CRediT authorship contribution statement

Qiyu Liu: Data curation, Investigation, Writing - original draft, Writing - review & editing, Formal analysis. **Tao Pu:** Data curation, Formal analysis, Investigation. **Xiaobo Zhou:** Data curation, Formal analysis, Investigation. **Jiaan Sun:** Data curation, Formal analysis. **Wei Yuan:** Methodology. **Sidi Zhang:** Methodology. **Mingxing Zhang:** Data curation, Formal analysis. **Meng Zhang:** Data curation, Formal analysis. **Jing Peng:** Data curation, Formal analysis. **Fuyou Li:** Conceptualization. **Xiaoyan Zhang:** Conceptualization, Writing - review & editing. **Congjian Xu:** Conceptualization, Supervision.

Declaration of competing interest

The authors declare the following financial interests/personal relationships which may be considered as potential competing interests: Qiyu Liu, Xiaobo Zhou, Fuyou Li, Xiaoyan Zhang and Congjian Xu has patent A tumor imaging and therapeutic probe targeting follicle-stimulating hormone receptor licensed to Obstetrics and Gynecology Hospital of Fudan University.

Data availability

Data will be made available on request.

Acknowledgements

This work was supported by the National Natural Science Foundation of China (82172747), the National Key R&D Program of China (2016YFC1303100), China Postdoctoral Science Foundation (2023M730121), Shanghai Clinical Research Center for Gynecological Diseases (22MC1940200) and Shanghai Urogenital System Diseases Research Center (2022ZZ01012).

Appendix A. Supplementary data

Supplementary data to this article can be found online at https://doi.org/10.1016/j.mtbio.2023.100904.

References

[1] R.L. Siegel, K.D. Miller, N.S. Wagle, A. Jemal, Cancer statistics, 2023, Ca-Cancer J. Clin. 73 (2023) 17–48.
[2] G. Corrado, V. Salutari, E. Palluzzi, M.G. Distefano, G. Scambia, G. Ferrandina, Optimizing treatment in recurrent epithelial ovarian cancer, Expert Rev. Anticancer Ther. 17 (2017) 1147–1158.
[3] S. Lheureux, M. Braunstein, A.M. Oza, Epithelial ovarian cancer: evolution of management in the era of precision medicine, Ca - Cancer J. Clin. 69 (2019) 280–304.
[4] C. Yang, B. Xia, Z. Zhang, Y. Zhang, G. Lou, W. Jin, Immunotherapy for ovarian cancer: adjuvant, combination, and neoadjuvant, Front. Immunol. 11 (2020), 577869.
[5] Z. Peng, M. Li, H. Li, Q. Gao, PD-1/PD-L1 immune checkpoint blockade in ovarian cancer: dilemmas and opportunities, Drug Discov. Today 28 (2023), 103666.
[6] Y. Klymenko, O. Kim, M.S. Stack, Complex determinants of epithelial: mesenchymal phenotypic plasticity in ovarian cancer, Cancers 9 (2017).
[7] A.M. Nick, R.L. Coleman, P.T. Ramirez, A.K. Sood, A framework for a personalized surgical approach to ovarian cancer, Nature Reviews, Clin. Oncol. 12 (2015) 239–245.
[8] R.N. Eskander, J. Kauderer, K.S. Tewari, R.S. Mannel, R.E. Bristow, D.M. O'Malley, et al., Correlation between Surgeon's assessment and radiographic evaluation of residual disease in women with advanced stage ovarian cancer reported to have undergone optimal surgical cytoreduction: an NRG Oncology/Gynecologic Oncology Group study, Gynecol. Oncol. 149 (2018) 525–530.
[9] K. Kleinmanns, V. Fosse, B. Davidson, E.G. de Jalón, O. Tenstad, L. Bjørge, et al., CD24-targeted intraoperative fluorescence image-guided surgery leads to improved cytoreduction of ovarian cancer in a preclinical orthotopic surgical model, EBioMedicine 56 (2020), 102783.
[10] R.R. Zhang, A.B. Schroeder, J.J. Grudzinski, E.L. Rosenthal, J.M. Warram, A. N. Pinchuk, et al., Beyond the margins: real-time detection of cancer using targeted fluorophores, Nat. Rev. Clin. Oncol. 14 (2017) 347–364.
[11] J. Shao, C. Ruan, H. Xie, Z. Li, H. Wang, P.K. Chu, et al., Black-phosphorus-incorporated hydrogel as a sprayable and biodegradable photothermal platform for postsurgical treatment of cancer, Adv. Sci. 5 (2018), 1700848.
[12] B. Li, E. Pang, S. Zhao, G. Deng, S. Wang, B. Wang, et al., Aggregation-enhanced photophysical performance of D-π-A structured hemicyanine for NIR-II fluorescent and photoacoustic imaging-guided photothermal therapy, Chemical & Biomedical Imaging 1 (2023) 541–549.
[13] L. Zhao, X. Zhang, X. Wang, X. Guan, W. Zhang, J. Ma, Recent advances in selective photothermal therapy of tumor, J. Nanobiotechnol. 19 (2021) 335.
[14] Y. Liu, P. Bhattarai, Z. Dai, X. Chen, Photothermal therapy and photoacoustic imaging via nanotheranostics in fighting cancer, Chem. Soc. Rev. 48 (2019) 2053–2108.
[15] L. Tu, Z. Liao, Z. Luo, Y.L. Wu, A. Herrmann, S. Huo, Ultrasound-controlled drug release and drug activation for cancer therapy, Explorations 1 (2021), 20210023.
[16] X. Zhao, C.X. Yang, L.G. Chen, X.P. Yan, Dual-stimuli responsive and reversibly activatable theranostic nanoprobe for precision tumor-targeting and fluorescence-guided photothermal therapy, Nat. Commun. 8 (2017), 14998.
[17] L.M. Randall, R.M. Wenham, P.S. Low, S.C. Dowdy, J.L. Tanyi, A phase II, multicenter, open-label trial of OTL38 injection for the intra-operative imaging of folate receptor-alpha positive ovarian cancer, Gynecol. Oncol. 155 (2019) 63–68.
[18] K.M. Sundaram, Y. Zhang, A.K. Mitra, J.K. Kouadio, K. Gwin, A.A. Kossiakoff, et al., Prolactin receptor-mediated internalization of imaging agents detects epithelial ovarian cancer with enhanced sensitivity and specificity, Cancer Res. 77 (2017) 1684–1696.
[19] H. Shi, Y. Sun, R. Yan, S. Liu, L. Zhu, S. Liu, et al., Magnetic semiconductor Gd-doping CuS nanoparticles as activatable nanoprobes for bimodal imaging and targeted photothermal therapy of gastric tumors, Nano Lett. 19 (2019) 937–947.
[20] A. Perales-Puchalt, N. Svoronos, M.R. Rutkowski, M.J. Allegrezza, A.J. Tesone, K. K. Payne, et al., Follicle-stimulating hormone receptor is expressed by most ovarian cancer subtypes and is a safe and effective immunotherapeutic target, Clin. Cancer Res. 23 (2017) 441–453.
[21] A. Radu, C. Pichon, P. Camparo, M. Antoine, Y. Allory, A. Couvelard, et al., Expression of follicle-stimulating hormone receptor in tumor blood vessels, N. Engl. J. Med. 363 (2010) 1621–1630.

[22] D.A. Modi, S. Sunoqrot, J. Bugno, D.D. Lantvit, S. Hong, J.E. Burdette, Targeting of follicle stimulating hormone peptide-conjugated dendrimers to ovarian cancer cells, Nanoscale 6 (2014) 2812–2820.
[23] X. Zhang, J. Chen, Y. Zheng, X. Gao, Y. Kang, J. Liu, et al., Follicle-stimulating hormone peptide can facilitate paclitaxel nanoparticles to target ovarian CarcinomaIn vivo, Cancer Res. 69 (2009) 6506–6514.
[24] L. Fan, J. Chen, X. Zhang, Y. Liu, C. Xu, Follicle-stimulating hormone polypeptide modified nanoparticle drug delivery system in the treatment of lymphatic metastasis during ovarian carcinoma therapy, Gynecol. Oncol. 135 (2014) 125–132.
[25] S. Cheng, Q. Liu, X. Zhou, Y. Gu, W. Yuan, W. Feng, et al., Reversible ratiometric probe combined with the time-gated method for AccurateIn vivo gastrointestinal pH sensing, ACS Appl. Mater. Interfaces 12 (2020) 25557–25564.
[26] T.A. Santa Coloma, B. Dattatreyamurty Jr., L.E. Reichert, A synthetic peptide corresponding to human FSH beta-subunit 33-53 binds to FSH receptor, stimulates basal estradiol biosynthesis, and is a partial antagonist of FSH, Biochemistry 29 (1990) 1194–1200.
[27] X. Jiang, H. Liu, X. Chen, P.H. Chen, D. Fischer, V. Sriraman, et al., Structure of follicle-stimulating hormone in complex with the entire ectodomain of its receptor, Proc. Natl. Acad. Sci. U. S. A. 109 (2012) 12491–12496.
[28] K. Urbanska, C. Stashwick, M. Poussin, D.J. Powell, Follicle-stimulating hormone receptor as a target in the redirected T-cell therapy for cancer, Cancer Immunol. Res. 3 (2015) 1130–1137.
[29] Z. Feng, H. Wen, R. Bi, X. Ju, X. Chen, W. Yang, et al., A clinically applicable molecular classification for high-grade serous ovarian cancer based on hormone receptor expression, Sci. Rep. 6 (2016), 25408.
[30] M. Lenhard, T. Lennerova, N. Ditsch, S. Kahlert, K. Friese, D. Mayr, et al., Opposed roles of follicle-stimulating hormone and luteinizing hormone receptors in ovarian cancer survival, Histopathology 58 (2011) 990–994.
[31] Z. Feng, H. Wen, X. Ju, R. Bi, X. Chen, W. Yang, et al., Expression of hypothalamic-pituitary-gonadal axis-related hormone receptors in low-grade serous ovarian cancer (LGSC), J. Ovarian Res. 10 (2017) 7.
[32] H. Hong, Y. Yan, S. Shi, S.A. Graves, L.K. Krasteva, R.J. Nickles, et al., PET of follicle-stimulating hormone receptor: broad applicability to cancer imaging, Mol. Pharm. 12 (2015) 403–410.
[33] M. Zhang, Q. Liu, M. Zhang, C. Cao, X. Liu, M. Zhang, et al., Enhanced antitumor effects of follicle-stimulating hormone receptor-mediated hexokinase-2 depletion on ovarian cancer mediated by a shift in glucose metabolism, J. Nanobiotechnol. 18 (2020) 161.
[34] G.M. van Dam, G. Themelis, L.M. Crane, N.J. Harlaar, R.G. Pleijhuis, W. Kelder, et al., Intraoperative tumor-specific fluorescence imaging in ovarian cancer by folate receptor-alpha targeting: first in-human results, Nat. Med. 17 (2011) 1315–1319.
[35] C.E.S. Hoogstins, Q.R.J.G. Tummers, K.N. Gaarenstroom, C.D. de Kroon, J.B.M. Z. Trimbos, T. Bosse, et al., A novel tumor-specific agent for intraoperative near-infrared fluorescence imaging: a translational study in healthy volunteers and patients with ovarian cancer, Clin. Cancer Res. 22 (2016) 2929–2938.
[36] J.L. Tanyi, L.M. Randall, S.K. Chambers, K.A. Butler, I.S. Winer, C.L. Langstraat, et al., A phase III study of pafolacianine injection (OTL38) for intraoperative imaging of folate receptor–positive ovarian cancer (study 006), J. Clin. Oncol. 41 (2023) 276–284.
[37] J.M. de Jong, J.P. Hoogendam, A.J.A.T. Braat, R.P. Zweemer, C.G. Gerestein, The feasibility of folate receptor alpha- and HER2-targeted intraoperative fluorescence-guided cytoreductive surgery in women with epithelial ovarian cancer: a systematic review, Gynecol. Oncol. 162 (2021) 517–525.
[38] L. Ceppi, N.M. Bardhan, Y. Na, A. Siegel, N. Rajan, R. Fruscio, et al., Real-time single-walled carbon nanotube-based fluorescence imaging improves survival after debulking surgery in an ovarian cancer model, ACS Nano 13 (2019) 5356–5365.
[39] F. Ren, Z. Jiang, M. Han, H. Zhang, B. Yun, H. Zhu, et al., NIR-II Fluorescence imaging for cerebrovascular diseases, View-China 2 (2021), 20200128.
[40] Y. Urano, M. Sakabe, N. Kosaka, M. Ogawa, M. Mitsunaga, D. Asanuma, et al., Rapid cancer detection by topically spraying a γ-glutamyltranspeptidase–activated fluorescent probe, Sci. Transl. Med. 3 (2011) 110ra119.
[41] D. Asanuma, M. Sakabe, M. Kamiya, K. Yamamoto, J. Hiratake, M. Ogawa, et al., Sensitive beta-galactosidase-targeting fluorescence probe for visualizing small peritoneal metastatic tumours in vivo, Nat. Commun. 6 (2015) 6463.
[42] A. du Bois, A. Reuss, E. Pujade Lauraine, P. Harter, I. Ray Coquard, J. Pfisterer, Role of surgical outcome as prognostic factor in advanced epithelial ovarian cancer: a combined exploratory analysis of 3 prospectively randomized phase 3 multicenter trials, Cancer 115 (2009) 1234–1244.
[43] S. Wang, X. Ma, X. Hong, Y. Cheng, Y. Tian, S. Zhao, et al., Adjuvant photothermal therapy inhibits local recurrences after breast-conserving surgery with little skin damage, ACS Nano 12 (2018) 662–670.
[44] T. Mantso, S. Vasileiadis, I. Anestopoulos, G.P. Voulgaridou, E. Lampri, S. Botaitis, et al., Hyperthermia induces therapeutic effectiveness and potentiates adjuvant therapy with non-targeted and targeted drugs in an in vitro model of human malignant melanoma, Sci. Rep. 8 (2018) 10716–10724.
[45] Z. Li, J. Deng, J. Sun, Y. Ma, Hyperthermia targeting the tumor microenvironment facilitates immune checkpoint inhibitors, Front. Immunol. 11 (2020), 595207.
[46] L. Huang, Y. Li, Y. Du, Y. Zhang, X. Wang, Y. Ding, et al., Mild photothermal therapy potentiates anti-PD-L1 treatment for immunologically cold tumors via an all-in-one and all-in-control strategy, Nat. Commun. 10 (2019) 4871.
[47] M. Chang, Z. Hou, M. Wang, C. Li, J. Lin, Recent advances in hyperthermia therapy-based synergistic immunotherapy, Adv. Mater. 33 (2021), e2004788.
[48] Q. Chen, L. Xu, C. Liang, C. Wang, R. Peng, Z. Liu, Photothermal therapy with immune-adjuvant nanoparticles together with checkpoint blockade for effective cancer immunotherapy, Nat. Commun. 7 (2016), 13193.
[49] H. Monaco, S. Yokomizo, H.S. Choi, S. Kashiwagi, Quickly evolving near-infrared photoimmunotherapy provides multifaceted approach to modern cancer treatment, View-China 3 (2022).
[50] Z. Lin, Z. Chen, Y. Chen, N. Yang, J. Shi, Z. Tang, et al., Hydrogenated silicene nanosheet functionalized scaffold enables immuno-bone remodeling, Explorations 3 (2023), 20220149.
[51] M. Ge, H. Guo, M. Zong, Z. Chen, Z. Liu, H. Lin, et al., Bandgap-engineered germanene nanosheets as an efficient photodynamic agent for cancer therapy, Angew. Chem. Int. Ed. 62 (2023), e202215795.
[52] Q. Yu, J. Zhou, H. Wang, Y. Liu, H. Zhou, B. Kang, et al., A multiple-response cascade nanoreactor for starvation and deep catalysis chemodynamic assisted near-infrared-II mild photothermal therapy, Chemical & Biomedical Imaging 1 (2023) 242–250.